Single-mode selection and axial mode control in a free-electron maser oscillator using a prebunched electron beam

M. Cohen,* A. Eichenbaum, H. Kleinman, D. Chairman, and A. Gover
Department of Physical Electronics, Tel-Aviv University, Ramat-Aviv, 69978, Israel
(Received 27 December 1995)

The effects of electron-beam prebunching on the radiation buildup process in a free-electron maser oscillator operating in the frequency range of 4–5 GHz were studied. An electron beam of 10 keV, 1 A was prebunched by means of a microwave tube section, accelerated to 70 keV, transported through a drift region by a solenoidal magnetic field and injected into a linearly polarized wiggler in which a free-electron laser interaction takes place. Single-frequency selection and locking due to electron-beam prebunching was demonstrated; we show that by tuning the electron-beam prebunching frequency we can set the oscillator frequency at any of the resonant frequencies of the cavity within the net gain bandwidth. An appreciable speedup of the oscillation buildup due to prebunching was also observed; the buildup time of radiation in the presence of prebunching is shortened compared to the case of the free-running oscillator. [S1063-651X(96)00609-5]

PACS number(s): 41.60.Cr, 42.50.Fx, 84.40.Ik

I. INTRODUCTION

In a free-electron laser (FEL) oscillator, as in any laser, the radiation may be self-excited and starts to grow spontaneously from noise if the round-trip small-signal gain of the radiation exceeds its round-trip loss [1]. Typically, the gain bandwidth is larger than the frequency interval between the natural frequencies of the resonant cavity. This means that a number of different longitudinal modes of the resonator compete with each other for extracting energy from the same electrons in the electron beam in the stimulated emission process. In the linear regime, when the radiation in the oscillator starts to grow, the radiation spectrum may be composed of a large number of different frequencies. However, as the signal grows further on and upon entering the nonlinear regime, negative coupling between the longitudinal modes increases the *effective gain* and enhances the buildup of the mode of highest power, suppressing the gain of the other modes whose power gets diminished, until a single-mode oscillation emerges [2] with extremely high coherence of the emitted radiation [3]. Under certain conditions (of strong pumping) the mode competition process may evolve into chaos and multifrequency noisy radiation output will emerge from the oscillator [2]. This mode competition process, which takes place during the oscillation buildup period of every FEL oscillator, has been the subject of recent theoretical and experimental investigations [2,4–6].

In oscillators that start the oscillation buildup process spontaneously from noise, the mode that has the highest gain will generally win the mode competition process. This conclusion is based on the assumption that the initial noise power is equally partitioned among the modes. This assumption is limited by the statistical nature of the noise source (shot noise and thermal noise) [5]. If a large number of modes satisfy the oscillation condition, there may be some uncertainty in the prediction of the evolving steady-state oscillation frequency. Such uncertainty also exists if there are other instabilities in the laser parameters (especially beam energy fluctuations). One way to overcome this uncertainty in the oscillation frequency and to determine it in advance is to inject sufficient initial excess power into the desired oscillator mode. Due to the nonlinear nature of the competition process, this mode may emerge a *winner* even if its linear gain is smaller than the gain of the other modes that satisfy the oscillation condition.

Oscillator frequency selection and single-mode locking by means of seed radiation injection or current modulation are well known techniques for enhancing the oscillation buildup process in oscillator resonators, for setting the oscillation frequency and for stabilizing it. These techniques have been demonstrated and are being used in microwave tubes [7–10] and in conventional lasers [11–14].

Frequency locking and mode selection by prebunching of the electron beam is a process that is different from seed radiation injection, which is the known way for priming a single mode in conventional laser oscillators. Electron-beam prebunching would be equivalent in conventional lasers to establishment of phase coherence in the polarization of the amplifying medium (superradiance). Periodic bunching [15–19] of the electron beam is an efficient way to enhance the radiation process in FELs since power emission is proportional to the square of the number of electrons. By comparison, spontaneous emission is linearly proportional to the number of oscillating electrons. From the practical point of view, frequency locking by use of electron-beam prebunching can be performed more easily than radiation seed injection because it is a unidirectional process, while in the seed radiation process it is impossible to inject the radiation without getting radiation coupled out or contributing insertion loss to the resonator.

The motivation for single-mode frequency locking may be a desire to tune to an exact and stable frequency (for a particular application or for facilitating coherent coupling of a number of radiation sources [8]). Furthermore, as shown in

*Permanent address: Nuclear Research Center–Negev, Physics Department, P.O. Box 9001, Beer-Sheva 84190 Israel. Electronic address: moshec@newton.bgu.ac.il

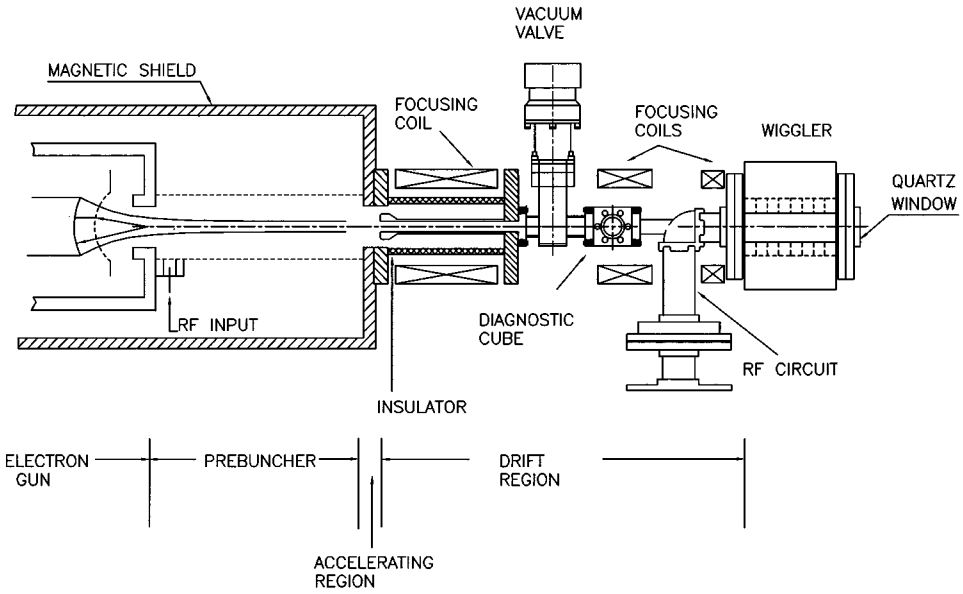

FIG. 1. Basic scheme of the prebunched beam FEM experiment.

[2], the highest gain mode is not necessarily the one that extracts the highest power out of the gain medium (the electron beam) at saturation and does not yield the highest oscillator power. It is usually desirable to excite a mode with a larger *detuning value* (which can be done by frequency locking) in order to operate the FEL at the highest energy extraction efficiency and highest power output [20].

II. THE FREE-ELECTRON MASER EXPERIMENTAL SETUP

A conspicuous feature of the present free-electron maser (FEM) experiment is the use of a unique electron-beam prebuncher employed to interfere in the FEL oscillation buildup process. In the present scheme, a section of a microwave wave tube is used to produce the bunched electron beam. The experimental setup of the prebunched electron-beam FEM is illustrated by Fig. 1.

The electron beam is produced by a Pierce-type thermionic electron gun and is prebunched by a section of a microwave tube operated at 10 kV, 1 A. The electromagnetic wave is absorbed at the end of the prebuncher while the bunched beam exits. The frequency and the amplitude of prebunching are controlled by the rf input signal to the prebuncher. The electron beam is accelerated to 70 keV in a short acceleration gap, transported through a drift section where a focusing solenoidal magnetic field is imposed, and injected into the wiggler. Elements for electron-beam diagnostic include a straight thin wire that allows an assessment of the transverse position and the dc current density distribution of the electron beam, and a fluorescent quartz screen used for viewing and to enable adjustment of the electron beam at the screen plane. These diagnostic elements can be shifted into and out of the beam line with precision linear motion feedthroughs. A capacitive button monitor is installed through a flange in the diagnostic cube and positioned 8 mm away from the electron-beam axis. It is used as a rf pickup that detects the envelope of the rf current component on the electron beam (proportional to the bunching amplitude). The voltage induced on the button was found to be proportional to the rf input power to the buncher. Table I contains the main parameters of the electron beam at the wiggler entrance plane.

The electron beam is injected into a planar wiggler, which consists of a stack of Sm-Co permanent magnets that are arranged in a Halbach configuration. Since the electron-beam energy is moderate and the current density in the beam is relatively high, horizontal focusing means along the wiggler are essential to overcome the space-charge forces and to keep the electron beam on the wiggler axis from excessive spreading. The wiggler parameters are presented in Table II. To attain a circular electron beam in the wiggler, equal focusing strength is required in both the vertical (x) and horizontal (y) dimensions ($k_{\beta x}=k_{\beta y}$). In the vertical dimension, natural focusing is provided by the wiggler itself. For electron-beam focusing in the lateral dimension of the planar wiggler, a scheme based on the use of two long permanent magnets at the sides of the wiggler was developed (see Fig. 2). The long magnets create a superimposed vertical magnetic field with a lateral gradient that provides electron focusing in the horizontal dimension [18]. The horizontal gradient of the vertical magnetic field that is required to satisfy

TABLE I. Electron-beam parameters at the wiggler entrance plane.

Electron-beam energy (spread)	Beam current	Beam diameter	Macropulse duration
$\mathcal{E}=70$ keV ($\frac{\sigma\epsilon}{\epsilon}\approx 0.5\%$)	$I_0=1$ A	$r_b=2$mm	$\tau=1$–20 μs

TABLE II. Planar wiggler parameters.

Wiggler field	Period length	Number of periods	Betatron wave number
$B_w = 300$ G ($a_w = 0.12$)	$\lambda_w = 4.4$ cm	$N_w = 17$	$k_{\beta x} = k_{\beta y} = 23.4$ rad/m

the condition of equal vertical and transverse focusing power is given by [21]

$$\alpha_R \equiv \frac{\partial B}{\partial x} = \frac{eB_w^2}{2mc\gamma\beta_{0z}}, \tag{1}$$

where m is the rest mass of the electron, $\beta_{0z} = v_{0z}/c$ with v_{0z} the axial velocity of the electron and c the velocity of light in vacuum, and γ is the *relativistic Lorentz factor* given by $(1 - v^2/c^2)^{-1/2}$. B_w is the peak value of the vertical component of the wiggler field and $\partial B/\partial x$ is the field gradient superimposed by the horizontal focusing magnets. For the present FEM experimental parameters, the required gradient is $\alpha_R = 4.9$ G/mm. The distance between the longitudinal magnets that produces the gradient α_R can be calculated from the expression [21]

$$D = \left[16 \frac{hd}{\pi} \frac{B_r}{\alpha_R} \right]^{1/3}, \tag{2}$$

where h, d, and B_r characterize the dimensions (cross section) and the residual field of the permanent magnet. With the magnet parameters employed in our experiment, we find from Eq. (2) that for equal horizontal and vertical focusing strengths the longitudinal magnets should be located a distance $D = 10.42$ cm apart.

In order to verify experimentally the effectiveness of the horizontal focusing electron-optical design, the electron-beam current density distribution at the wiggler exit was viewed on a fluorescent quartz screen using a charge coupled device (CCD) camera. Single-frame CCD displays of the fluorescent spot are shown in Figs. 3(a)–3(c) for various cases of horizontal spacing between the longitudinal magnets D'. Figure 3(a) depicts the horizontal divergence of the electron beam when no focusing means in the lateral dimension

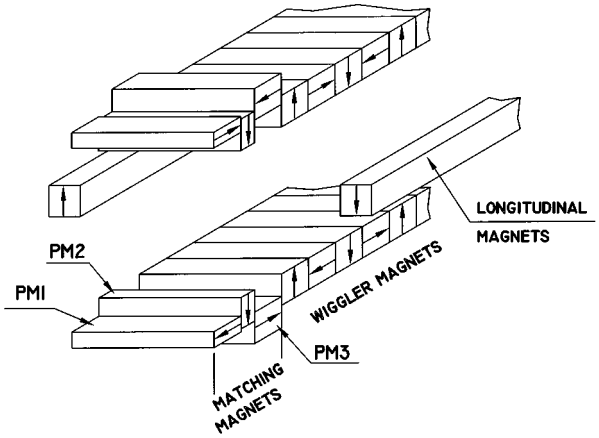

FIG. 2. Sketch of the planar wiggler with two longitudinal magnets for horizontal focusing and corrections magnets at both ends of the wiggler.

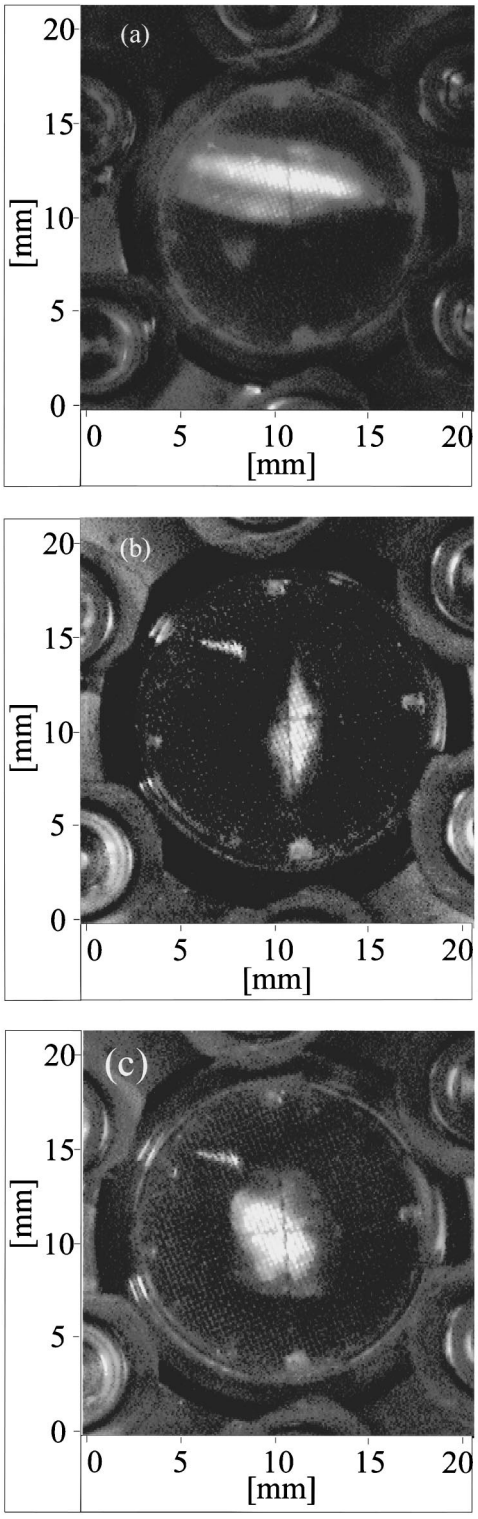

FIG. 3. Electron-beam pulse current density distribution viewed by a CCD camera at the wiggler exit (a) without horizontal focusing ($D' \gg D$), (b) with horizontal overfocusing ($D' < D$), and (c) with proper horizontal focusing ($D' = D$).

TABLE III. Microwave circuit (TE_{10} mode) parameters.

Waveguide dimensions	Length of resonator	Cutoff frequency	Frequency (at maximum linear gain)	Internal loss (per round-trip)	Power filling factor
$a\times b=47.55\times 22.15$ mm^2	$L_c=1.05$ m	$f_{c_{nm}}=3.15$ GHz	$f_0=4.535$ GHz	$L_i=0.065$ dB	$A_e/A_{em}=0.024$

are employed ($D'\gg D$). In Fig. 3(b) the focusing strength in the horizontal dimension is stronger than the vertical focusing strength of the wiggler ($D'<D$). When the long magnets were placed with the theoretical interspace ($D'=D$) corresponding to equal horizontal and vertical focusing strength [Eqs. (1) and (2)], a circular confined beam was achieved, as shown in Fig. 3(c). Good agreement was obtained between experiment, theory, and numerical simulations of the electron-beam transport.

A rectangular waveguide was used for the FEM resonator. The end of the bent output waveguide section and the front end were terminated with reflectors in order to produce a resonator configuration. The electron beam was injected into the resonator through a nonradiating 9-mm-diam aperture in the waveguide bend, which produced no rf power coupling out of the resonator and caused internal rf power reflections of less than 5% [22].

III. FREE-RUNNING OSCILLATOR

For a rectangular waveguide resonator of dimensions $b<a<L_c$, where a and b are the transverse dimensions and L_c is the length of the resonator, the TE_{10} mode is the fundamental transverse mode. The intersections between the waveguide dispersion curves and the electron-beam line describe the operation points at which the FEL interaction occurs. The parameters of the resonator for the TE_{10} mode are given in Table III. For these parameters, there is no intersection with higher-order modes and therefore only the fundamental transverse mode TE_{10} can be excited.

We use the dispersion relation of the waveguide $\omega=\sqrt{c^2k_z^2+\omega_{c_{nm}}^2}$ to determine the eigenfrequencies. For any eigenfrequency, the mode propagation constant must satisfy $k_z=l\pi/L_c$, where l is the longitudinal mode number. This condition defines the resonant frequencies of the rectangular waveguide resonator, i.e.,

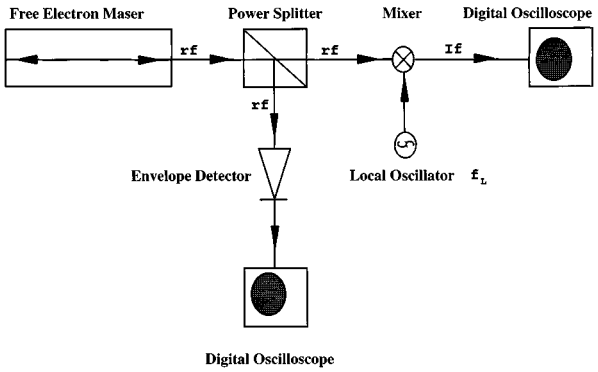

FIG. 4. Block diagram for measuring the power and the frequency of the FEM output.

$$f_{nml}=\sqrt{\left(\frac{cl}{2L_c}\right)^2+f_{c_{nm}}^2}, \tag{3}$$

where $f_{c_{nm}}=c\sqrt{(n/2a)^2+(m/2b)^2}$ is the cutoff frequency. The frequency spacing between the resonant axial modes of the waveguide cavity is approximately constant and is given by

$$\Delta f=\frac{v_g}{2L_c}, \tag{4}$$

where $v_g=c\sqrt{1-(f_{c_{nm}}/f_0)^2}$ is the group velocity of the radiation mode. For the TE_{10} mode and the parameters given in Table III, $\Delta f\approx 100$ MHz and therefore the transit time for one round-trip in the cavity is approximately $T_r=1/\Delta f\approx 10$ ns.

The power envelope and the rf wave form of the output signal from the free-electron maser were measured using a setup shown by the block diagram in Fig. 4. The power emitted from the partially transmitting output coupling mirror at the end of the waveguide is divided by a power splitter. A calibrated crystal detector is used in one branch to measure the signal power envelope. The other branch is used for frequency heterodyning measurement. The output signal is mixed with an external rf signal at frequency f_{LO}, which is generated by a very stable local oscillator.

In Fig. 5 we display the wave forms of the electron-beam current pulse [trace (1)] and the detected power envelope of the resonator output signal [trace (2)]. The unbunched current pulse, passing through the resonator, causes initially an exponential buildup of the rf power in the resonator, starting

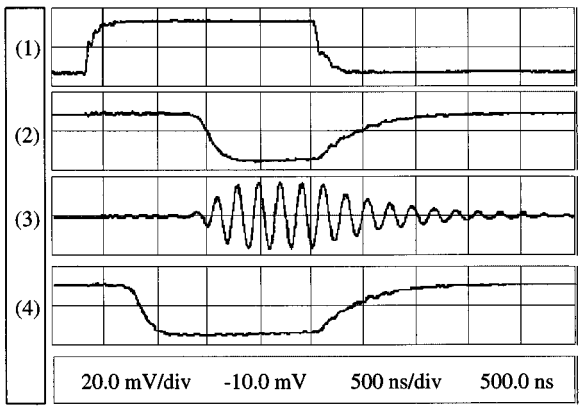

FIG. 5. Electron-beam current pulse and the FEM output signals evolution in time. Trace (1) is the electron-beam current pulse. Trace (2) is the rf output signal without prebunching the electron beam. Trace (3) is the IF signal at a frequency of 4.75 MHz while the local oscillator frequency is 4.540 00 GHz. Trace (4) is the rf output signal corresponding to the electron-beam bunching frequency that is close to the free-running oscillator frequency.

from an initial noise level. The radiation buildup process continues until the circulating power reaches saturation; at the steady-state level the single-pass saturated FEM gain just equals the total round-trip cavity losses. The oscillation buildup time as shown in the oscilloscope trace (2) is about $\tau_b = 1200$ ns. A constant output signal is obtained after $N = \tau_b / T_r \approx 120$ round-trips. This number of round-trips is relatively small, corresponding to an appreciable net linear gain per path.

The intermediate frequency (IF) signal is shown as trace (3) of Fig. 5. The local oscillator frequency is $f_{LO} = 4.540\,00$ GHz and the IF signal frequency is $f_{IF} = 4.75$ MHz. These frequencies correspond to an accurately measured free-running oscillator frequency of $f_0 = f_{LO} - f_{IF} = 4.535\,25$ GHz.

In the initial experiments we did not have accurate measure of the transmission factor of the output mirror of the resonator. We can only deduce its level from the measurements of the internal losses of the resonator (which were made beforehand) and the decay time of the radiation in the cavity.

The total loss of the circulating power in the resonator (per round-trip) is

$$L = L_i + (1 - R), \tag{5}$$

where L_i is the internal (Ohmic wall) losses of the waveguide and $1 - R$ is the power out-coupling coefficient of the front mirror. The stored power decay constant (Γ_c) and decay time (τ_c) can be expressed in terms of the loss factor

$$\Gamma_c = \frac{1}{\tau_c} = \frac{L}{T_r}. \tag{6}$$

The internal loss factor was measured directly [by a transmission experiment where we define the loss to be $L = -10\log_{10} P_{\text{trans}} / P_{\text{in}}$ (dB)]. We found that the circulating power was reduced by $L_i = 0.065$ dB per round-trip, which means 1.48% power loss per round-trip (this corresponds to a quality factor of the unloaded resonator $Q_u = \omega_0 \tau_{ci} = \omega_0 L_i / T_r = 19\,000$).

The total loss factor of the loaded cavity ($R < 1$) can be inferred from the measure power decay time depicted by trace (2) of Fig. 5: $\tau_c = 395$ ns (this corresponds to a quality factor of $Q_L = \omega_0 \tau_c = 11\,255$). Note that the *field amplitude* decay time measure from the IF signal trace (3) in Fig. 5 is 800 ns, corresponding to $2\tau_c$ (twice the power decay time), as expected.

The total loss per round-trip L for the loaded waveguide resonator can be calculated from Eq. (6) and we find $L = 0.11$ dB, which means 2.5% power loss per round-trip. Using the loaded and unloaded loss values $L = 0.11$ dB and $L_i = 0.065$ dB we deduce [Eq. (5)] that the output coupling loss is $T = 1 - R = 0.045$ dB, which means 1.03% power transmission per round-trip. This corresponds to a power reflection coefficient of $R = 98.97\%$. It is clear that in these initial measurements the oscillator is operated in the high-reflectivity limit with the less than optimal output coupling. The output power that was measured on a calibrated crystal diode in this limit was about 250 mW. Much higher power levels were obtained in subsequent experimental measurements with increased outcoupling [23].

IV. SINGLE-PASS SMALL-SIGNAL GAIN

Using a linear theoretical model for FEL, [24,25] the small signal gain of the FEM in the low gain collective (Raman) regime per single path is described analytically by the expression

$$G(L_w) - 1 \equiv \frac{\Delta P(L_w)}{P(0)} = \kappa \mathcal{F} \theta_p^2 L_w^3 F(\overline{\theta, \theta_{p_r}}), \tag{7}$$

where $\kappa = (1/4)(\overline{v_w}/v_{0z})^2 (\omega/c)^2 / k_z$ is the coupling parameter, $\overline{v_w}$ is the rms wiggling velocity, and ω and k_z are the frequency and the axial wave number of the radiation, respectively; $\mathcal{F} \equiv A_e / A_{em}$ is the power filling factor that describes the overlap of the electron beam with the radiation field in the transverse plane; $\theta_p = \omega_{\text{pl}} / v_{0z}$ is the relativistic electron-beam plasma wave number; and L_w is the wiggler length. The gain function $F(\theta, \theta_{p_r})$ is defined by

$$F(\overline{\theta, \theta_{p_r}}) = \frac{1}{2\overline{\theta_{p_r}}} \left\{ \frac{\sin^2[(\overline{\theta} + \overline{\theta_{p_r}})/2]}{[(\overline{\theta} + \overline{\theta_{p_r}})/2]^2} - \frac{\sin^2[(\overline{\theta} - \overline{\theta_{p_r}})/2]}{[(\overline{\theta} - \overline{\theta_{p_r}})/2]^2} \right\}, \tag{8}$$

where $\overline{\theta_{p_r}} = \sqrt{r}\,\theta_p L_w$ is the plasma wave number modified by a geometric reduction factor r [26] and normalized to the wiggler length, $\overline{\theta(\omega)} = [\omega / v_{0z} - k_w - k_z(\omega)] L_w$ is the normalized detuning parameter, and k_w is the wiggler wave number. $G(L_w) = P(L_w)/P(0)$ describes the unsaturated power gain of the FEL amplifier per single path at the output end $z = L_w$.

The theoretical small-signal gain is now compared with the experimental measurements. Based on the set of parameters that are given in Tables I–III we calculate the small-signal single-pass gain as a function of the radiation frequency and present it in Fig. 6. The resonator longitudinal modes falling under the gain curve and the total loss (including internal and external losses) are also depicted in Fig. 6. The resonant frequencies under the gain curve are nearly equispaced. They correspond to the longitudinal modes of the transverse mode TE_{10}. Their frequencies were determined from Eq. (3) and are listed in Table IV. Note that seven longitudinal modes satisfied the oscillation condition.

For an assumption of a plasma reduction factor $r = 0.35$, the gain curve corresponds to operation in the marginal collective (Raman) regime (i.e., $\theta_{p_r} = 8.5 > \pi$). In this regime, the gain and attenuation regions, corresponding to FEL interaction with the slow and fast Langmuir plasma waves of the beam respectively, are well separated. These regions of interaction with the negative and positive energy plasma waves are described by the first and second terms on the right-hand side of Eq. (8), respectively. Note that for the other limit ($\theta_{p_r} \ll \pi$) the gain curve reduces to the well known S-shaped curve of the Compton regime [25]. The lower gain curve is an enlargement of the positive gain region in the complete gain-attenuation curve. In Fig. 6 we

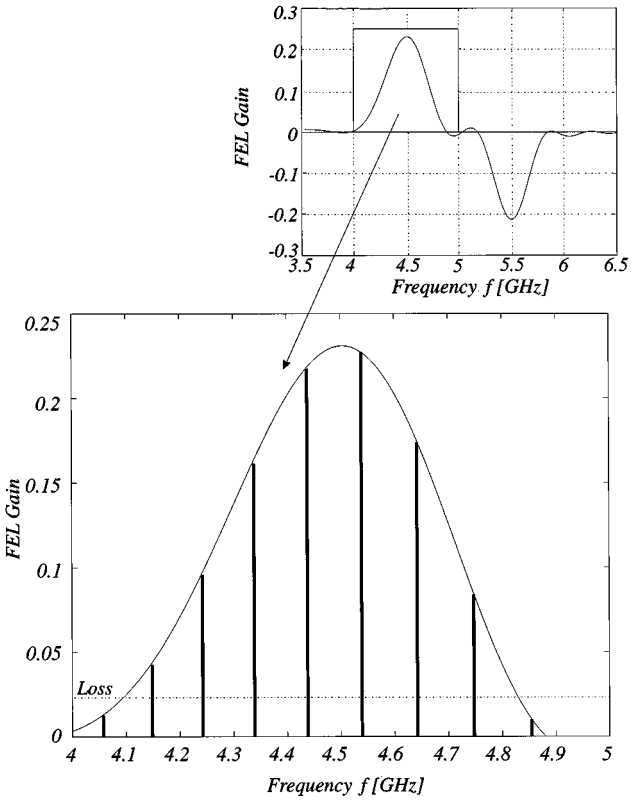

FIG. 6. FEM gain $[G(L_w)-1]$ vs the frequency. The lower figure is an enlargement of the interest frequency range in the upper figure. The maximum gain is achieved at 4.539 00 GHz. The round-trip loss was estimated from the decay time of the energy in the resonator and found to be 2.5% (the Q_L factor is about 11 255).

may note that the frequency of the maximum gain mode agrees with the measured frequency of the free-running oscillator.

In Fig. 7 the linear gain measurements for some of the eigenmodes are compared to the theoretical gain curve. The single-pass gain is measured experimentally in the FEM oscillator configuration from the rate of rise of the output signal with time. We shall exploit the single-frequency selection effect (an effect described in detail later) to force the oscillator to oscillate at desired eigenfrequencies within the net gain bandwidth. This way gain measurements could be made at five frequency data points by measurement of the logarithmic slope of the signal traces of the oscillation buildup periods (see Fig. 7). The measurements exhibit agreement between experiment and theory. A FEM amplifier configuration is now being implemented and detailed linear gain measurements are planned to be provided in a future paper.

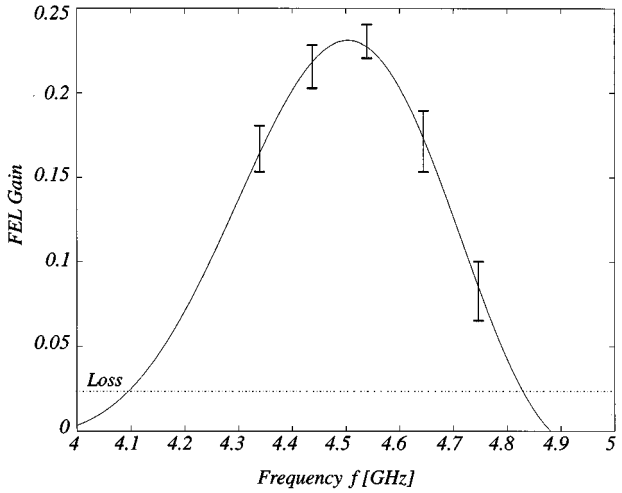

FIG. 7. FEM single-pass small-signal gain. The experimental data were obtained in the oscillator configuration where the power output can be viewed as being the regenerative amplified reproduction of the input signal injected by the prebunched electron beam.

V. SINGLE-FREQUENCY EVOLUTION

The FEM oscillator described in this article is driven by an electron-beam current pulse of relatively long duration and is therefore capable in principle of establishing single-frequency oscillation. We wish to consider whether the FEM oscillates in a single mode at a single frequency or in many modes at once. The axial cavity mode whose frequency is located closest to the center of gain curve (see Fig. 6) has the highest gain and will thus normally be the one emerging from the competition with other modes as the single surviving mode. However, there are several factors that may prevent evolution of the single-frequency oscillation. One factor may be the insufficient time of the pulse to complete the mode competition process (which continues after saturation [2]). If radiation outcoupling is too small one may also fall into an unstable region where single-mode operation is never attained.

TABLE IV. Resonant frequencies of the FEM oscillator. The experimental frequencies were obtained via the single-frequency locking effect. The electron-beam prebunching is used to force the oscillator to achieve steady state of a single-mode operation at any eigenmode in the net gain bandwidth.

Mode number l	Theory [Eq. (3)] f (GHz)	Experiment f (GHz)	Inaccuracy (%)
19	4.1485	4.1333	0.37
20	4.2424	4.2339	0.20
21	4.3388	4.3345	0.10
22	4.4377	4.4349	0.06
23	4.5390	4.5352	0.08
24	4.6423	4.6373	0.11
25	4.7476	4.7389	0.18

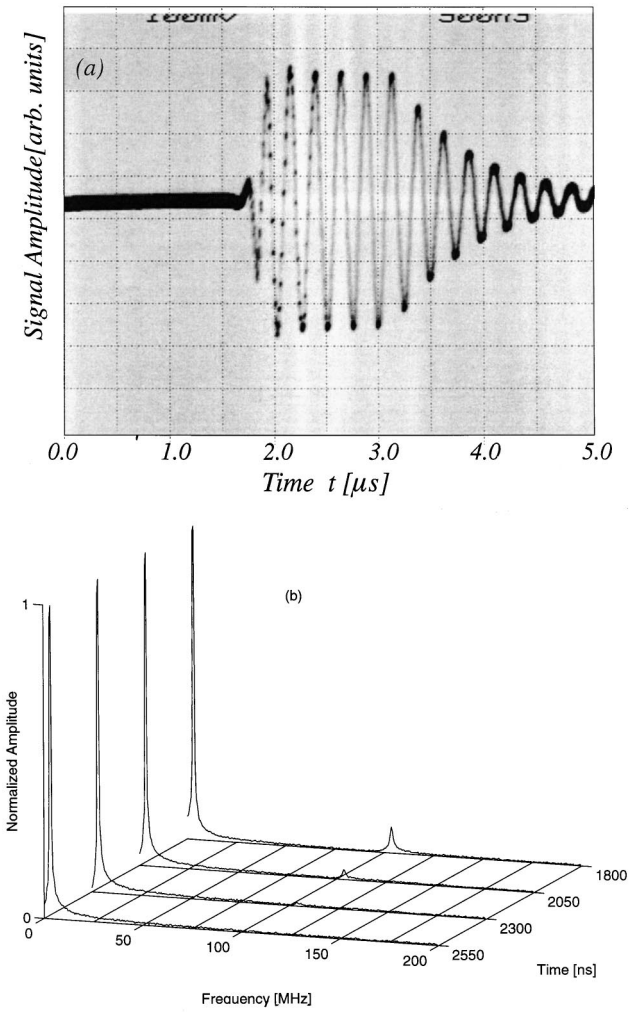

FIG. 8. (a) FEM output signal evolution in time without prebunching the electron beam. The oscilloscope trace is an IF signal at a frequency of 3.75 MHz, where the local oscillator frequency is 4.539 00 GHz. The small periodic irregularities along the trace correspond to an adjacent competing longitudinal mode. (b) IF spectrum of the FEM output showing the evolution in time for $t=1.8,\ 2.05,\ 2.3$, and 2.55 μs. The injection of the electron beam current is at $t=1.0$ μs.

A Tektronix fast digitizer oscilloscope with a bandwidth of 0.5 GHz is used to resolve a wide frequency range of the output radiation pulse spectrum. With this bandwidth the digitizer oscilloscope is capable of resolving at least five axial modes oscillating simultaneously. Using a measurement setup as shown in Fig. 4, the FEM output radiation is mixed with a stable local oscillator signal that is tuned to a frequency $f_{\mathrm{LO}}=4.539\,00$ GHz, which is close to the free-running oscillator frequency. The amplitude of the FEM output signal at the IF frequency is shown in Fig. 8(a) as it evolves in time. The signal amplitude evolution vs time as shown in this figure depicts the nonlinear regime competition of the axial modes in the oscillator cavity where the small periodic irregularities along the trace indicate the presence of the adjacent competing longitudinal mode.

In Fig. 8(a) one can see that single-frequency operation is achieved about 800 ns after saturation is reached (the small periodic irregularities along the trace disappeared). This steady state of a single-frequency operation is attained a short time after a mode competition process, in which the mode that corresponds to the free-running oscillator mode and has the highest linear growth rate is accompanied by at least one adjacent axial mode with a relatively small amplitude. Note that the local oscillator frequency ($f_{\mathrm{LO}}=4.539\,00$ GHz) and the IF signal frequency that can be measured from the trace of Fig. 8(a) ($f_{\mathrm{IF}}=1/T_{\mathrm{IF}}=3.75$ MHz) can be used to deduce the free-running oscillator frequency $f_0=f_{\mathrm{LO}}-f_{\mathrm{IF}}=4.535\,25$ GHz.

Fourier transformation of the IF output signal is shown in Fig. 8(b). This figure shows the spectral components of the IF signal at times $t=1.80,\ 2.05,\ 2.30$, and 2.55 μs, where the injection of the electron-beam current is at $t=1.0$ μs. For the sake of clarity we present only 200 MHz of the spectrum bandwidth. This analysis reveals two harmonic components with appreciable amplitudes as compared to other modes. In these spectra we found that the higher peak is at IF frequency $f_{\mathrm{IF}}=3.75$ MHz and the low decaying peak is at a frequency $f_{\mathrm{IF}}+\Delta f=104.05$ MHz. These modes correspond to two adjacent longitudinal modes: the free-running oscillator mode that oscillates at a frequency $f_0=f_{\mathrm{LO}}-f_{\mathrm{IF}}=4.535\,25$ GHz with a steady amplitude and an adjacent mode that oscillates at a frequency $f_{-1}=f_{\mathrm{LO}}-f_{\mathrm{IF}}-\Delta f=4.434\,95$ GHz with a small decaying amplitude. In Fig. 8(b) the spectrum of the signal 800 ns after saturation has begun, contains only a single large-amplitude mode, while the small-amplitude satellite mode is suppressed.

VI. EFFECTS OF ELECTRON-BEAM PREBUNCHING

If, by prebunching of the electron beam at the frequency of one of the resonator modes, enough power can be induced into that mode (in comparison to the spontaneous power), one may interfere in the mode competition process that evolves in the free-running oscillator and dictate the oscillator mode and frequency at steady state. In Fig. 9(a) we present the FEM oscillator output (IF signal) for the case where the electron beam is prebunched at the frequency of the mode of highest gain. The rf input power to the prebuncher was about 10 mW. Fourier analysis of the IF output signal at saturation (recorded with the 0.5-GHz bandwidth scope) is shown in Fig. 9(b). This figure shows the spectrum of the IF signal at times $t=1.50,\ 1.75,\ 2.00$, and 2.25 μs, where the injection of the electron-beam current is at $t=1.0$ μs. One can see that the spectrum of the signal immediately after saturation has begun contains a single harmonic component. In general, a prebunching power level of the order of several microwatts was sufficient to exhibit a stable equilibrium of single-mode operation.

Single-mode priming by prebunching the electron beam enhances the oscillation buildup rate of the radiation in the cavity. When the oscillation starts from the initial spontaneous-emission (noise) level, the radiation builds up exponentially and reaches, for the parameters of our experiment, a saturation power level within 1000 ns from the time of injection of the electron-beam current into the cavity, as shown by traces (1) and (2) of Figs. 5 and 8(a). If the rf signal frequency of the prebuncher is set at the frequency of the free-running oscillator mode, the oscillation buildup time shortens significantly. The buildup time in the experiments

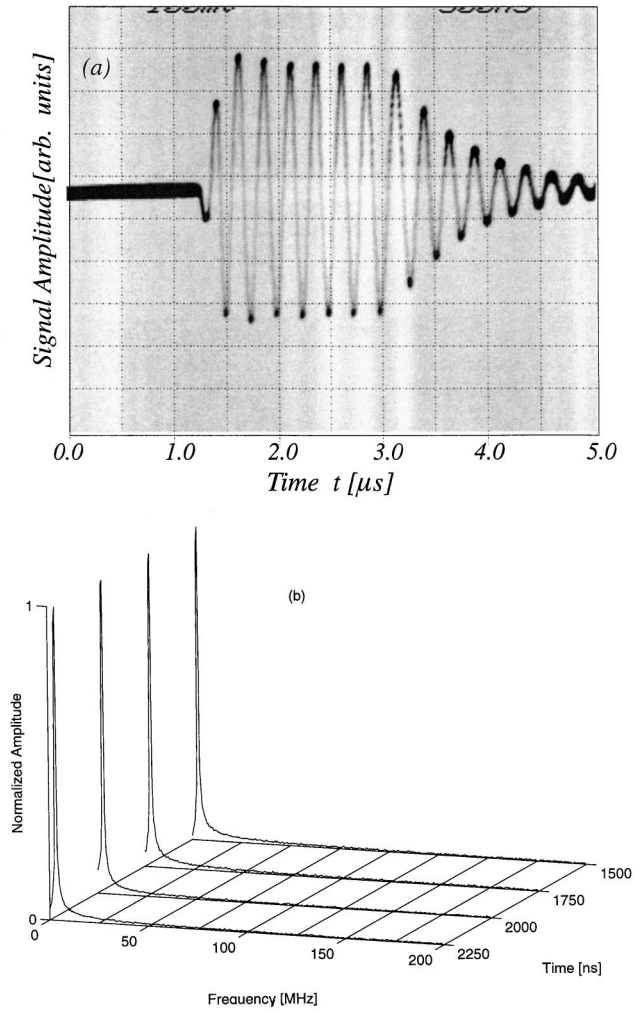

FIG. 9. (a) FEM output signal evolution in time with a prebunched electron beam. The trace is an IF signal at a frequency of 3.75 MHz, where the local oscillator frequency is 4.539 00 GHz. (b) IF spectrum of FEM output showing single-mode operation. The injection of the electron beam current is at $t=1.0$ μs.

depicted in trace (4) of Figs. 5 and 9(a) is about 500 ns (for a prebuncher rf input power of 10 mW). In Sec.VII we show that similar results are observed also at other eigenfrequencies within the net gain bandwidth of the FEM.

For a low-gain FEL oscillator we can make a model of the radiation buildup process in the linear growth stage (before the onset of saturation) as a regenerative amplifier. The growth in circulating power in one round-trip, starting from initial power level $P_{\rm in}$ at time $t=0$, is

$$P(T_r)=P_{\rm in}Ge^{-\Gamma_c T_r}, \tag{9}$$

where $G=P_{\rm out}/P_{\rm in}$ is the single-pass small-signal net gain of the FEM [Eq. (7)] and $\Gamma_c=\tau_c^{-1}$ is the cavity decay rate that takes into account the reflectivity of the output end of the resonator and waveguide losses [see Eqs. (5) and (6)] and T_r is the resonator round-trip traversal time. The net growth after N round-trips will be given by

$$P(t)=P_{\rm in}G^{t/T_r}e^{-\Gamma_c t}, \tag{10}$$

where $t=NT_r$. The total power buildup from $P_{\rm in}$ to the oscillator saturation power level P_s is given by the approximate expression

$$P_s=P_{\rm in}\exp\left[\left(\frac{\ln G}{T_r}-\frac{1}{\tau_c}\right)\tau_b\right], \tag{11}$$

where τ_b is the oscillation buildup time. Solving Eq. (11) for the buildup time τ_b we find

$$\tau_b=\frac{T_r}{\ln G-\dfrac{T_r}{\tau_c}}\ln\left(\frac{P_s}{P_{\rm in}}\right), \tag{12}$$

where the ratio T_r/τ_c represents the loss in the cavity per round-trip. Note that for a free-running oscillator, the input power level $P_{\rm in}$ to the resonator is the spontaneous emission power $P_{\rm in}=P_{\rm sp}$, while for an oscillator driven by a prebunched electron beam, the input power level is the superradiance emission power $P_{\rm in}=P_{\rm sp}$, which depends on the prebunching current amplitude. In our first experiment we found that the small-signal gain is $G\approx 1.2$ per single path, the resonator round-trip traversal time is $T_r=10$ ns, and the energy decay time is about $\tau_c=400$ ns. The buildup time of the radiation in the free-running FEM oscillator is 1200 ns [see trace (2) of Fig. 5] and the output power that was measured on a calibrated crystal diode in this case was about 250 mW. Substituting these parameters into Eq. (12) and solving it for the input power, we conclude that the spontaneous-emission power is on the order of 20 nW.

The spectral density of the spontaneous radiation can be also calculated by using the expression [21]

$$\frac{dP_\nu}{d\omega}=\left(\frac{eI_0}{16\pi}\right)\left(\frac{\sqrt{\mu_0/\epsilon_0}}{A_{em}\cos\Theta_\nu}\right)\left(\frac{a_w^2}{\gamma_0^2\beta_{0z}^2}\right)L_w^2\,\mathrm{sinc}^2\left(\frac{\overline{\theta_\nu}(\omega)}{2}\right), \tag{13}$$

where $\sqrt{\mu_0/\epsilon_0}/A_{em}\cos\Theta_\nu$ is the mode impedance parameter and $a_w=eB_w/mck_w$ is the wiggler parameter. The spontaneous-emission power at the output of the resonator is obtained by integration of the power density over the linewidth of the resonant frequency (the longitudinal mode with the highest linear growth rate). This linewidth is given by $\delta f=\Delta f/F$, where $F=\pi\sqrt{R}/(1-R)$ is the finesse of the resonator [1] and Δf is given by Eq. (4). For the fundamental transverse mode TE_{10} is found to be on the order of 50 nW, in agreement with our previous experimental measurement.

We measured the buildup time as a function of the rf input power to the prebuncher for two resonant modes: the free-running oscillator mode and the adjacent (higher-frequency) mode. The experimental results are presented in Fig. 10. In this figure we can see that the buildup time ranges between ≈ 1.2 μs and ≈ 0.6 μs (i.e., saturation will be exceeded after 120 and 60 round-trips, respectively).

The experimental measurement of the buildup time shows that the logarithm of the ratio $P_s/P_{\rm in}$ varies from $\ln(P_s/P_{\rm in})=19$ (for 1.2 μs) to $\ln(P_s/P_{\rm in})=9.5$ (for 0.6 μs). Since the output power from the resonator is of the order of hundreds of milliwatts, one can find that the superradiance emission power due to prebunched electron beam ranges from 20 nW to 50μW. The relatively low power level for the

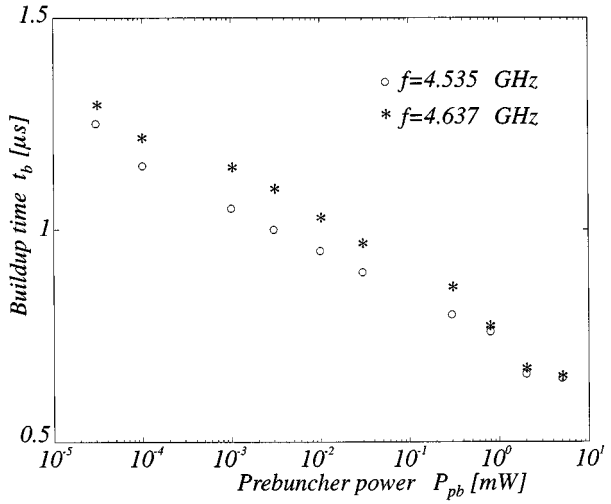

FIG. 10. Oscillation buildup time vs the prebunching input power. The buildup times were measured for the free-running oscillation frequency and for the adjacent axial mode.

superradiance emission is a consequence of the small bunching amplitude attained at the low rf input power to the prebuncher (up to 10 mW). This power level is, however, significantly higher than the noise level and is sufficient to interfere strongly in the mode competition process.

VII. OSCILLATOR MODE SELECTION AND SINGLE-FREQUENCY LOCKING

The FEM oscillator dynamics with prebunching at eigenfrequencies other than the free-running oscillator frequency is described next. The frequency of the prebuncher was scanned manually throughout the net gain bandwidth of the FEM to demonstrate single-frequency locking and mode selection. The IF output signal from the mixer was displayed on a fast digitizer oscilloscope. With the prebunching frequency close to one of the eigenfrequencies of the resonator, we observed single-frequency locking effect of the oscillator frequency. This phenomenon is observed at all resonator eigenfrequencies in the gain bandwidth. Furthermore, the oscillation buildup time shortens significantly relative to the free-running oscillation buildup time, as explained in Sec. VI. In Fig. 10 we plotted the experimental measurements of the buildup time for the 4.64-GHz eigenmode, which was selected and locked by the prebunched electron beam. This is shown by the asterisk data point, in addition to the data points of the maximum gain frequency 4.535 GHz shown by open circles (which was discussed in Sec. VI). The buildup time of lower gain modes was longer for the same prebunching power, as expected.

By scanning the rf buncher frequency, it was found that the prebunched electron beam causes seven different longitudinal modes to be excited with a spacing of about 100 MHz in agreement with Eq. (4) and the mode map of Fig. 6. We noted that even a very weak input signal to the prebuncher was sufficient to turn the selected axial mode into the dominant one in the FEM cavity.

Seven modes falling under the FEM gain curve are listed in Table IV. The second column contains the theoretical eigenfrequencies, which were obtained by solving Eq. (3) for

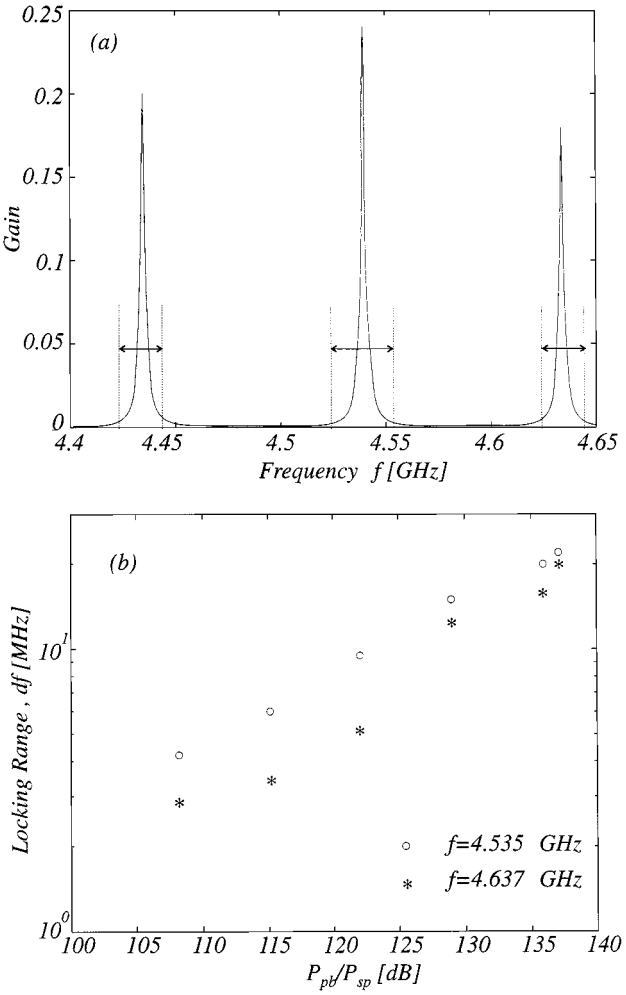

FIG. 11. Single-frequency locking range. (a) The locking range (vertical dashed lines) is illustrated for three eigenmodes of the resonator cavity: the free-running oscillator mode and its two adjacent axial modes. The cavity modes are plotted in scale according to their small-signal gain. (b) The width of the single-frequency locking range vs the prebunching power (P_{PB}) normalized to the noise power level (P_{sp}).

$l=19$–25. The third column presents the experimental resonant frequencies, which were measured via oscillator single-mode selection (frequency locking) effect.

The oscillator frequency can be locked to one of these cavity modes within a certain range called *the locking range*. The locking effect depends on the level of the prebunching power of the electron beam relative to that of the start-up noise and on the frequency detuning of the prebunching frequency off the oscillator eigenmode frequency. Inside the locking range, the maser output consists entirely of the single cavity mode, the closest to the prebunching frequency. The locking range can be explained in terms of wave frequency broadening for a finite time duration: for instance, a 10-MHz detuning of the prebuncher frequency corresponds to half of one rf period slippage between the prebunching signal and the resonator mode frequency during a 50-ns period: five resonator round-trip traversal times. The physical significance of this is that the mode growth in five round-trips is large enough, so that it is not subsequently suppressed by the prebunched beam, which during this time

slipped out of phase with the radiation signal.

The locking range of a single frequency around the free-running oscillator frequency [see Fig. 11(a)] for a prebunching input power of 10 mW, as measured experimentally, is about 10 MHz at each side of the eigenmode. Figure 11(b) shows measurements of the width of the single-frequency locking range as a function of the input power level to the prebuncher (P_{PB}) normalized to the noise power level (P_{sp}).

We also observed that at certain high level of input power to the prebuncher an overlap between the locking range of two adjacent cavity modes occurs and both are excited and reach saturation. This interesting phenomenon still has to be investigated more carefully while studying the mode competition process and mode dynamics.

ACKNOWLEDGMENTS

This work is part of a FEL development project supported by the Israel–U.S. Binational Science Foundation, the Israel Academy of Sciences, the Meyer Foundation, and the Israeli Ministries of Energy and Science.

[1] A. Yariv, *Quantum Electronics* (Wiley, New York, 1989).
[2] T. M. Antonsen, Jr. and B. Levush, Phys. Rev. Lett. **62**, 1488 (1989).
[3] A. Gover, A. Amir, and L. R. Elias, Phys. Rev. A **35**, 164 (1987).
[4] L. R. Elias, G. Ramian, J. Hu, and A. Amir, Phys. Rev. Lett. **57**, 424 (1986).
[5] R. J. Harvey and F. A. Dolezal, Appl. Phys. Lett. **53**, 1150 (1988).
[6] T. S. Chu, F. V. Hartemann, B. G. Danly, and R. J. Temkin, Phys. Rev. Lett. **72**, 2391 (1994).
[7] J.C. Slater, *Microwave Electronics* (Van Nostrand, Princeton, 1950).
[8] V. L. Granatstein, in *High Power Microwave Sources*, edited by V. L. Granatstein and I. Alexeff (Artech House, Boston, 1987), Chap. 5.
[9] A. H. McCurdy and C. M. Armstrong, Phys. Fluids B **3**, 212 (1991).
[10] R. P. Fischer, A. W. Fliflet, W. M. Manheimer, B. Levush, T. M. Antonsen, Jr., and V. L. Granatstein, Phys. Rev. Lett. **72**, 2395 (1994).
[11] R. Adler, Proc. IEEE **61**, 1380 (1973).
[12] R. H. Pantell, Proc. IEEE **53**, 474 (1965).
[13] H. A. Haus, H. Statz, and I. W. Smith, IEEE J. Quantum Electron. **QE-21**, 78 (1985).
[14] D. C. Gerstenberger, G. E. Tye, and R. W. Wallace, Opt. Lett. **16**, 992 (1991).
[15] C. Leibovitch, K. Xu, and G. Bekefi, IEEE J. Quantum Electron. **QE-24**, 1825 (1988).
[16] G. Dearden *et al.*, Nucl. Instrum. Methods Phys. Res. Sect. A **318**, 230 (1992).
[17] I. Schnitzer and A. Gover, Nucl. Instrum. Methods Phys. Res. Sect. A **237**, 124 (1985).
[18] M. Cohen *et al.*, Nucl. Instrum. Methods Phys. Res. Sect. A **358**, 82 (1995).
[19] D. A. Jaroszynski, R. J. Bakker, A. F. G. van der Meer, D. Oepts, and P. W. van Amersfoort, Phys. Rev. Lett. **71**, 3798 (1993).
[20] M. Cohen, A. Eichenbaum, M. Arbel, D. Ben-Haim, H. Kleinman, M. Draznin, A. Kugel, Y. Yakover, and A. Gover, Phys. Rev. Lett. **74**, 3812 (1995).
[21] M. Cohen, Ph.D. thesis, Tel-Aviv University, 1995 (unpublished).
[22] D. Ben-Haim, M.Sc. thesis, Tel-Aviv University, 1994 (unpublished).
[23] A. Avramovich, Y. Pinhasi, M. Cohen, I. M. Yakover, A. Eichenbaum, H. Kleinman, A. Gover, B. Levush, T. M. Antonsen, and V. L. Granatstein, Nucl. Instrum. Methods Phys. Res. Sect. A **375**, 164 (1996).
[24] A. Gover and A. Yariv, J. Appl. Phys. **16**, 121 (1978).
[25] E. Jerby and A. Gover, IEEE J. Quantum Electron. **QE-21**, 1041 (1985).
[26] Y. Pinhasi and A. Gover, Phys. Rev. E **48**, 3925 (1993).